Supporting information for:

# Zwitterions in 3D Perovskites: Organosulfide-Halide Perovskites

Jiayi Li,[1] Zhihengyu Chen,[2] Santanu Saha,[3] James Utterback,[4] Michael L. Aubrey,[1] Rongfeng Yuan,[4] Hannah L. Weaver,[4] Naomi S. Ginsberg,[4,5,6,7,8] Karena W. Chapman,[2] Marina R. Filip*[,3] and Hemamala I. Karunadasa*[,1,9]

[1]*Department of Chemistry, Stanford University, Stanford, California 94305, United States*
[2]*Department of Chemistry, Stony Brook University, Stony Brook, New York 11794, United States*
[3]*Department of Physics, University of Oxford, Oxford OX1 3PU, United Kingdom*
[4]*Department of Chemistry, University of California, Berkeley, California 94720, United States*
[5]*STROBE, National Science Foundation Science and Technology Center, University of California Berkeley, Berkeley, California 94720, United States*
[6]*Department of Physics, University of California Berkeley, Berkeley, California 94720, United States*
[7]*Materials Science Division and Molecular Biophysics and Integrated Bioimaging Division, Lawrence Berkeley National Laboratory, Berkeley, California 94720, United States*
[8]*Kavli Energy NanoSciences Institute at Berkeley, Berkeley, California 94720, United States*
[9]*Stanford Institute for Materials and Energy Sciences, SLAC National Accelerator Laboratory, Menlo Park, CA 94025, United States*

**hemamala@stanford.edu,*
**marina.filip@physics.ox.ac.uk*

**Table of Contents**

## 1. Materials

General methods: All syntheses were conducted in a $N_2$-filled glovebox unless otherwise noted. All reagents were purchased from commercial vendors and used as received. Solvents were of reagent grade or higher purity. Solvents were dried using a JC Meyer solvent purification system. Powders of $(MA)PbX_3$ (X = Cl, Br)[1] and of $(Pb_2Cl_2)(CYS)_2PbCl_4$[2] were synthesized as previously reported. Abbreviations used: CYS = cysteamine, CYS·HCl = cysteamine hydrochloride, MA = methylammonium, DMF = *N*,*N*-dimethylformamide, PMMA = poly(methyl methacrylate).

### Synthesis of (CYS)$PbCl_2$

*Powders*: Solid $PbCl_2$ (169 mg, 0.608 mmol) was combined with 10 mL of DMF in a 20 mL scintillation vial. Solid CYS (50.0 mg, 0.648 mmol) was combined with 1 mL of DMF in a 4 mL scintillation vial. The two vials were heated at 150 $^0$C for 15 minutes until all solids fully dissolved. Then the CYS solution was added dropwise into the stirred $PbCl_2$ solution. The solution turned yellow instantly and an orange solid precipitated. The mixture was stirred at 150 $^0$C for 40 minutes. The product was then separated by hot filtration and dried under reduced pressure overnight. Anal. Calcd. for $C_2H_7NSPbCl_2$: C, 6.76%; H, 1.99%; N, 3.94%. Found: C, 6.77%; H, 1.92%; N 3.84%.

*Single crystals*: Solid $PbCl_2$ (85 mg, 0.30 mmol) was combined with 10 mL of DMF in a 20 mL scintillation vial. After the solid fully dissolved in DMF at 150 $^0$C, the solution was filtered through a glass filter paper into a clean vial. Solid CYS (12 mg, 0.16 mmol) and CYS·HCl (18 mg, 0.16 mmol) were combined and dissolved with 1 mL of DMF in a 4 mL scintillation vial at 150 $^0$C. Then, the ligand solution was slowly added to the $PbCl_2$ solution. Yellow square crystals formed after the mixture was left undisturbed for 20 minutes. Most of the solution was decanted at 150 $^0$C and then the mixture allowed to cool to room temperature.

### Synthesis of (CYS)$PbBr_2$

Solid $PbBr_2$ (233 mg, 0.635 mmol) and CYS (50.0 mg, 0.648 mmol) were separately combined with 0.5 mL of DMF in 4 mL scintillation vials. The two vials were heated at 145 $^0$C for 3 minutes until all solids fully dissolved. Then the CYS solution was added dropwise into the stirred $PbBr_2$ solution. The solution turned yellow instantly and a red solid precipitated. The mixture was kept at 145 $^0$C for 3 minutes. The product was separated by hot filtration and dried under reduced pressure overnight. This method produces ca. 5% of the intergrowth impurity phase (see main text) evident in PXRD data. Small variations in temperature or heating time led to different amounts of this impurity phase. Anal. Calcd. for $C_2H_7NSPbBr_2$: C, 5.41%; H, 1.59%; N, 3.15%. Found: C, 5.50%; H, 1.56%; N, 3.27%.

## 2. Methods

### Single-crystal X-ray diffraction (SC-XRD)

Crystals were kept in a minimal amount of mother liquor and transferred to a glass slide containing Paratone-N® oil shortly after synthesis. A small fragment of a large crystal was used to avoid twin boundaries. Crystals were coated with Paratone-N oil, attached to a Kapton loop, and transferred to a Bruker D8 Venture diffractometer equipped with a Photon 100 CMOS detector. The mounted crystal was enveloped by a flow of $N_2$ and did not show significant decay during data collection. Frames were collected using $\omega$ and $\varphi$ scans and the unit-cell parameters were refined against all data. Data were integrated and corrected using SAINT V8.38A for Lorentz and polarization effects.[3] The absorption corrections were performed using SADABS-2016/2. Space-group assignments were based upon systematic absences, *E*-statistics, agreement factors for equivalent reflections and successful refinement of the structures. The structure was solved using the intrinsic phasing method implemented in SHELXT-2014.[4] The solution was refined against all data using the SHELXL-2018/3[5] software package and OLEX2.[6]

Considering the similar X-ray absorption cross sections of S and Cl, SC-XRD cannot reliably refine the occupancies of S and Cl. Therefore, the anion-site occupancy was defined as 2/3 Cl and 1/3 S based on the formula of $(CYS)PbCl_2$. The *R-3c* space group only exhibits one unique halide site position, which indicates disordered Cl and S. The disorder of S in the structure extends to disorder of the organoammonium tail of CYS as well. To account for the disordered organic component, a solvent mask function of OLEX2 was applied to improve the solution.[7] A solvent mask was calculated and 138 electrons were found per unit cell. This is consistent with the presence of $C_2NH_7$ per formula unit, which accounts for 156 electrons per unit cell.

**Powder X-ray diffraction (PXRD)**

PXRD data were collected using a Bruker D8 Advance Diffractometer equipped with a Cu source ($K\alpha_1$ = 1.54060 Å, $K\alpha_2$ = 1.54443 Å, $K\alpha_2/K\alpha_1 = 0.5$), fixed divergence slits with a nickel filter and a LYNXEYE 1D detector. The instrument was operated in a Bragg-Brentano geometry with a step size of 0.02°. Fine power samples were dispersed in toluene and transferred to a clean glass slide. The measurements were conducted under ambient atmosphere and the samples were brought from the glovebox immediately prior to the measurements. Simulated powder patterns were calculated directly from the crystallographic information files (CIFs) using the Mercury software.

**X-ray photoelectron spectroscopy (XPS)**

XPS data were measured using a PHI Versaprobe 3, equipped with a focused Ar ion gun (FIG) and electron gun. Finely ground powders of $(CYS)PbX_2$ (X = Cl, Br) and $(Pb_2Cl_2)(CYS)_2PbCl_4$ were prepared on electrical tape (2 mm × 2 mm). Survey scans were collected with a pass energy of 224 eV from 1100 eV to 0 eV. High-resolution scans were collected with a pass energy of 55 eV for C 1s, Pb 4f, S 2p, Cl 2p, and Br 3d signals. To minimize charging effects, the samples were neutralized using a FIG and electron gun. The high-resolution scans were calibrated using C 1s as the reference peak. The molar elemental ratios were determined by integrating peak areas from the high-resolution scans. The asymmetrical shape of the S 2p peak is caused by two closely spaced spin-orbit components ($2p_{1/2}$ and $2p_{3/2}$).

**Proton nuclear magnetic resonance ($^1$H NMR)**

$^1$H NMR spectra were recorded in a DCl solution in $D_2O$ (20 wt.%) using a 400 MHz Varian NMR spectrometer. Solid $(CYS)PbX_2$ was mixed with 1 mL of the DCl solution and allowed to sit for 1 h. The solution was then filtered, and the filtrate was analyzed by NMR.

**Pair distribution function (PDF) analysis**

The X-ray ($\lambda$ = 0.2115 Å) total scattering experiment was performed at beamline 11-ID-B, Advanced Photon Source, Argonne National Laboratory. 2D diffraction images were integrated to 1D data arrays using GSAS-II.[8] Reciprocal space data in $Q$ were converted to PDF by xPDFsuite.[9] Crystal structure modelling and refinement are powered by PDFgui.[10] Differential envelope density (DED) analysis was performed using a reported method.[11] This analysis maps the difference between the observed and calculated structure envelope densities, providing information of the position and approximate occupancy of guest molecules in the cavities. Combination of PDF[12] and DED was applied to locate the organoammonium tail of cysteamine in the unit cell.

The structures of (CYS)$PbX_2$ in the *R-3c* space group were refined with PDF data to get the unit-cell parameters and local coordination. In the model, S atoms occupy one third of the anion sites uniformly. This residual in the fitting (Figure S2) gives information of atomic distances between the organoammonium tails and between the tail and the perovskite framework. Acquiring the DED between the refined structures from PDF fitting and directly rebuilt structures from PXRD patterns maps out the extra electron density in the unit cell, which is located in the center of the cavity (Figure S3). In the optimized PDF fitting, a virtual atom (K) with large atomic displacement parameters is added to the center of the cavity to model the organoammonium tail of cysteamine. This combination of PDF and DED confirms that the organic ligand resides in the center of the A-site cavity. The larger $R_w$ for (CYS)$PbBr_2$ is attributed to the greater difference in the Pb–Br and Pb–S bond lengths (compared to Pb–Cl/S) in the single-anion-site model. The longer Pb–Br and (trans) Br···Br distances are responsible for the misfits at ~3 and 6 Å. The experimental PXRD data and simulated patterns from the PDF models agree well (Figure S4).

### Diffuse reflectance spectroscopy

Diffuse reflectance measurements were conducted using a Shimadzu UV-2600 spectrometer equipped with an integrating sphere. The spectra were collected with a reflective backing of compressed $BaSO_4$ mixed with samples. The spectra were converted to pseudo-absorbance spectra using the Kubelka-Munk transformation.[13]

### Photoluminescence spectroscopy

Room-temperature steady-state emission spectra were measured on powders mounted on quartz slides using a Horiba Jobin-Yvon Spex Nanolog fluorimeter equipped with a 450-W xenon lamp and R928P detector. For low-temperature emission spectra, the powder samples were prepared by mixing a suspension of the perovskites with a solution of PMMA in toluene. This slurry was then allowed to dry at room temperature and cooled to 80 K in a Janis ST-100 cryostat.

### Time correlated single photon counting (TCSPC)

TCSPC was performed in a home-built confocal microscope with a 63 × 1.4NA PLAN APO Leica objective (HC PL APO 63×/1.40 oil CS2, Leica Material #11506350). The few-ps excitation laser pulse trained at 200 kHz was derived from a third-harmonic noncollinear optical parametric amplifier (NOPA; Light Conversion), pumped by a 10 W Light Conversion PHAROS regeneratively amplified laser system with a fundamental wavelength of 1030 nm. The excitation pulse was centered at 530 nm with a bandwidth set to 20 nm. The beam was fiber-coupled into single-mode polarization-maintaining fiber to produce a high-quality Gaussian mode and was circularly polarized before entering the objective. The pump beam is focused to a spot size of ~250 nm FWHM (full width at half-maximum). Photoluminescence was collected through the same objective and transmitted through the dichroic routing mirror for the pump pulse (T600lpxr-UF2), then focused onto a single photon counting avalanche photodiode (SPAD) (Prof. Alberto Tosi, SPAD lab, Politecnico di Milano; PicoQuant) through a 605–665 nm bandpass filter (ET635/60 from Chroma). The counts from the SPAD were sent to a PicoQuant PicoHarp 300 for TCSPC. Electronic noise is the major source of the overall instrument response function (IRF), whose width is ~120 ps. TCSPC was performed at two pump powers, 2.4 nW and 0.23 nW, and the decay traces shared the same decay time constant. This corresponds to 17 and 1.6 $\mu W/cm^2$, respectively.

The sample is the same as the one used for stroboSCAT as described below. Care was taken to collect data while exciting and probing far from the edges of the cubic crystals and from twin planes.

## Stroboscopic optical scattering (stroboSCAT) measurements

The experimental setup for stroboscopic optical scattering (stroboSCAT) microscopy measurements has previously been described in detail.[14] Briefly, two laser diodes were used for the pump (LDH-D-C-470, PicoQuant) and the probe (LDH-D-C-640, PicoQuant) with center wavelengths of 470 and 635 nm, respectively. These were controlled by a laser driver PDL 828-S "SEPIA II" equipped with two SLM 828 driver modules and a SOM 828-D oscillator from PicoQuant. We used a laser repetition rate of 100 kHz, with the pump modulated at 660 Hz, while the pump-probe delay times were controlled electronically using the driver with 20 ps resolution. Both pump and probe beams were spatially filtered through 25 μm pinholes. The pump beam was telescoped to a ~6 mm diameter, while the probe beam was telescoped to 1 mm and focused into the back focal plane of the objective of a home-built microscope using an f = 300 mm wide-field lens. The two beams were combined using a long-pass filter (DMLP505, Thorlabs), and a 50/50 beamsplitter reflected both beams into a high numerical aperture (1.4 NA) oil-immersion objective (Leica HC PL APO 63×/1.40 NA) and onto the sample, resulting in an overlapped focused pump and wide-field probe illumination, respectively. The focused pump beam had a spot size of 278 nm (FWHM) at the sample plane. Probe light reflected from the sample was collected through the objective, isolated from pump scatter with a band-pass filter (FLH635-10, Thorlabs), and focused onto a charged metal oxide semiconductor (CMOS) detector with 5.86 μm square pixels triggered at 660 Hz (PixeLINK PL-D752, equipped with a Sony IMX 174 global shutter sensor) using an $f = 500$ mm lens placed one tube length (200 mm) away from the back focal plane of the objective. The total magnification is 63×500/200 = 157.5, giving 37.2 nm/pixel. stroboSCAT images were generated by taking the difference between pump-on and pump-off raw pixel intensities, normalized to the raw pump-off intensities, yielding $\Delta R/R$ contrast images. Setup automation and data acquisition were implemented in LabVIEW 2014 64-bit. Data analysis and plotting were performed using a combination of ImageJ (Fiji)[15] and Origin. Experiments were conducted at 295 K. The spatially integrated signal decay and mean-squared expansion curves were both independent of pump power over $2\sigma$-integrated fluences of 114–446 μJ/cm$^2$.

Samples were directly deposited onto coverslips in air. Care was taken to collect data while exciting and probing far from the edges of the cubic crystals and from twin planes.

## Computational methodology

*Computational Details*: All density functional theory (DFT) calculations have been carried out using the Quantum Espresso package (version 6.5),[16] within the Perdew-Burke-Ernzerhof (PBE) parametrization of the generalized gradient approximation (GGA).[17] We used the Optimized Norm Conserving Vanderbilt (ONCV) pseudopotentials[18] as found on the Pseudo Dojo repository[19] constructed for the PBE functional. We used scalar relativistic ONCV potentials for all geometric relaxations and the fully relativistic pseudopotentials (including spin-orbit coupling) for all electronic structure calculations. We used a kinetic energy cutoff of 70 Ry and a $\Gamma$-centered Monkhorst-Pack(MP)[20] 6 × 6 × 2 k-point grid for the Brillouin zone (BZ) sampling for all calculations of (CYS)$PbX_2$ and its counterpart $CsPbX_3$. We adopted a $\Gamma$-centered MP 8 × 8 × 8 grid for all calculations of orthorhombic $CsPbX_3$.

The density of states was calculated with a $\Gamma$-centered MP grid of 16 × 16 × 4 and 24 × 24 × 24 for (CYS)$PbX_2$ and orthorhombic $CsPbX_3$, respectively, with a gaussian smearing of 0.005 Ry. The effective mass was calculated via 2nd-order finite difference (5 stencil) on a reciprocal space grid of 0.02 Bohr$^{-1}$ using the effective mass calculator utility.[21]

To construct the atomic models of (CYS)PbX$_2$ used in our first principles calculations, we used lattice parameters and atomic positions as determined experimentally by pair distribution function analysis and relaxed only the atomic positions of the organoammonium tail of CYS until forces on the constituent atoms were smaller than 0.0001 Ry/Bohr. Full details of the construction of the disordered models of (CYS)PbX$_2$ are described below. For CsPbX$_3$, we used experimental structures reported for CsPbCl$_3$ and CsPbBr$_3$.[22]

*Structural Model for (CYS)PbX$_2$ (X = Cl, Br)*: The crystal structure of the disordered (CYS)PbX$_2$ (X = Cl, Br) is measured experimentally as a rhombohedral structure. The anion sites are partially occupied by S (33.3%) and halide Cl or Br (66.6%). In the structural models we build for DFT calculations, we keep the inorganic framework of the perovskite fixed and work on constructing the position and orientation of the molecule inside the perovskite A-site cavity. Importantly, in all our structural models we impose periodic boundary conditions, and work within a unit cell of 84 atoms (6 formula units), as determined experimentally.

To model the S/X occupation in (CYS)PbX$_2$, we started with an ordered configuration in which the two S atoms bonded to a single Pb atom are always diagonally opposite (*trans* coordination). We then constructed the arrangement of the organic tail CH$_2$CH$_2$NH$_3$ attached to S in a multistep relaxation procedure to obtain the zwitterionic arrangement of CYS, keeping the inorganic atomic sites and the lattice parameters fixed, as follows: i) we attached CH$_3$ (C$_1$) to S forming S-CH$_3$ and relaxed it; ii) we then removed one H from C$_1$ and attached another CH$_3$ (C$_2$) to C$_1$ forming S-CH$_2$-CH$_3$ and relaxed C$_2$ only; iii) we repeated the same process of removing H from C$_2$ and adding NH$_3$ (N$_1$) to C$_2$ forming S-CH$_2$-CH$_2$-NH$_3$ and relaxed N$_1$ only, and iv) we finally relaxed the obtained CH$_2$CH$_2$NH$_3$ tail attached to S. The relaxed model structure obtained in this multistep procedure is a rhombohedral supercell with 6 formula units. The transformed cubic supercell of the obtained rhombohedral cell is displayed in Figure S8.

*Structural Model for Cs(HS)PbX$_2$ (X = Cl, Br)*: We checked that our choice of S/X arrangement does not affect the main conclusions of our calculations via two tests. First, we constructed a model structure in which the zwitterionic CYS is replaced by Cs$^+$ and HS$^-$, keeping the structure of the inorganic network unchanged (Figure S10A, the structure is hereafter labeled as Cs(HS)PbX$_2$-*trans*). After relaxing the positions of the Cs and H atoms, we calculated the electronic band structure and found virtually no difference between the (CYS)PbX$_2$ and Cs(HS)PbX$_2$-*trans* band structures close to the band edges, as shown in Figure S10.

Second, we took the Cs(HS)PbX$_2$-*trans* structure thus constructed and exchanged the positions of one S (and respective H atom bound to it) with a neighboring X atom, and relaxed the Cs and H ions again, as shown in Figure S10B (labelled as Cs(HS)PbX$_2$-*cis* and *trans*). This results in a *cis* arrangement of two S atoms coordinated to Pb in one of the octahedra in the supercell. We once again observed no difference in the band edges of the band structure, as shown in Figure S10. Furthermore, both tests yielded band gaps for the Cs-based models within ~0.12 eV of those calculated for (CYS)PbX$_2$ and follow the same trend with respect to their respective halide composition. These systematic tests indicate that our conclusions are not sensitive to the choice of S/X configuration.

**Stability tests**

Thermogravimetric analyses (TGA) were conducted with a Netzsch TG 209 F1 Libra Thermo-Microbalance at a heating rate of 1 °C/minute from room temperature to 900 $^0$C under N$_2$ flow, using ca. 10-20 mg samples in alumina crucibles. An empty alumina crucible was used as correction before the sample measurement. The decomposition temperature ($T_d$) is defined as the temperature corresponding to 5% mass loss.

To study humidity stability, powders of (CYS)$PbX_2$ were placed on clean glass slides and transferred to a platform inside a glass jar loaded with DI water to keep the relative humidity (RH) maintained at 100% in the closed system. The jar was put inside a drawer to minimize light exposure.

To study the thermal stability in air, samples were placed on a metal pie block, which was kept at 60 °C. PXRD patterns were recorded to monitor decomposition using the same measurement parameters.

## 3. Supplementary Discussion

### Modeling two diffusivities in stroboSCAT measurements

The spatially integrated carrier relaxation exhibits a multicomponent decay trace, including a nanosecond component that overlaps the TCSPC decay trace for the first ~1 ns as well as a longer-lived, broad decay component whose half-life is in the range of ~100 ns. This suggests that the stroboSCAT signal decays in part by the same relaxation pathway observed by the PL emission but has an additional contribution due to the state that follows from the nonradiative decay. This lingering signal could be due to trapped carriers, the band-edge carriers that do not get trapped, or a rise in temperature due to nonradiative relaxation,[14,23,24] but the present experiments do not distinguish these cases.

In the main text, we focused on the narrow time window from 100 ps to 1 ns. Here we fit this behavior with a phenomenological model that assumes an exponential transition from $D_{\text{fast}}$ to $D_{\text{slow}}$ with time constant $\tau$: $D(t) = D_{\text{fast}}e^{-t/\tau} + D_{\text{slow}}(1 - e^{-t/\tau})$ to cover the whole time window. This gives a mean-squared expansion of $\sigma^2(t) - \sigma^2(0) = 2\tau(D_{\text{fast}} - D_{\text{slow}})(1 - e^{-t/\tau}) + 2D_{\text{slow}}t$,[25,26] which was used to fit the data, giving $D_{\text{fast}} = 6(1)\times10^{-2}$ cm$^2$/s, $D_{\text{slow}} = 1.5(2)\times10^{-3}$ cm$^2$/s, and $\tau = 0.4(1)$ ns. $D_{\text{fast}}$ is consistent with the value determined from 100 ps to 1 ns time window (described in the main text). $D_{\text{slow}}$, on the other hand, is on the same order of magnitude as reports of both trapped-carrier diffusion[25] and thermal diffusion[27] in metal halide perovskites. Because the measurement is in principle sensitive to both electronic carriers and thermal effects, we cannot conclusively assign this $D_{\text{slow}}$ to one process of the other.

### Thermal stability

A thermal decomposition pathway for (MA)$PbX_3$ is to form MA·X salts (volatile) and $PbX_2$ in the first step.[28] Similarly, TGA analysis (1 °C/minute) shows two smaller steps of mass loss below 300 °C, corresponding to the ligand loss in (CYS)$PbX_2$. Table S6 compares the theoretical values of $PbX_2$ weight percentages in the four perovskites with the experimental residue percentages after ligand loss. For (CYS)$PbBr_2$, the sublimation of $PbBr_2$ starts at ca. 500 °C. For (CYS)$PbCl_2$, the PXRD pattern of the decomposition product at 350 °C shows $PbCl_2$ and some amount of PbS, which indicates ligand decomposition to form PbS. The decomposition temperatures (95% mass) of (CYS)$PbX_2$ (ca. 200 °C) are slightly lower compared to those of (MA)$PbX_3$ (301 °C and 248 °C for X = Cl and Br, respectively), possibly due to the higher volatility of CYS compared to $CH_3NH_3\cdot X$ or the thermal decomposition of CYS.

## 4. Supplementary Data

**Table S1.** Crystallographic data for (CYS)PbCl$_2$

| | |
|---|---|
| Compound | (CYS)PbCl$_2$ |
| Empirical formula | $C_2NH_7PbSCl_2$ |
| Formula weight (g/mol) | 355.24 |
| Temperature (K) | 100 |
| Crystal system | Trigonal |
| Space group | *R*-3*c* |
| *a* (Å) | 7.9907(4) |
| *b* (Å) | 7.9907(4) |
| *c* (Å) | 19.7849(11) |
| Volume (Å$^3$) | 1094.04(13) |
| *Z* | 6 |
| Density, calc. (g/cm$^3$) | 3.235 |
| Absorption coefficient. (mm$^{-1}$) | 24.014 |
| *F*(000) | 792 |
| Crystal size (mm$^3$) | 0.02 × 0.02 × 0.01 |
| Radiation | Mo Kα ($\lambda$ = 0.71073 Å) |
| 2$\theta$ range (°) | 7.186 to 57.466 |
| Index ranges | $-10 \leq h \leq 10$,<br>$-10 \leq k \leq 10$,<br>$-26 \leq l \leq 26$ |
| Reflections collected/unique | 13141/320 |
| Completeness to $\theta_{max}$ | 0.996 |
| Max. and min. transmission | 0.4028, 0.3098 |
| Data/restraints/parameters | 320/0/8 |
| Goodness-of-fit on $F^2$ | 1.133 |
| Final *R* indices [$I > 2\sigma(I)$]$^a$ | $R_1 = 0.0193$<br>$wR_2 = 0.0468$ |
| *R* indices (all data)$^a$ | $R_1 = 0.0233$<br>$wR_2 = 0.0483$ |
| Largest diff. peak/hole (e/Å$^3$) | 0.85, –0.90 |

$^aR_1 = \Sigma||F_o| - |F_c||/\Sigma|F_o|$, $wR_2 = [\Sigma w(F_o^2 - F_c^2)^2/\Sigma(F_o^2)^2]^{1/2}$

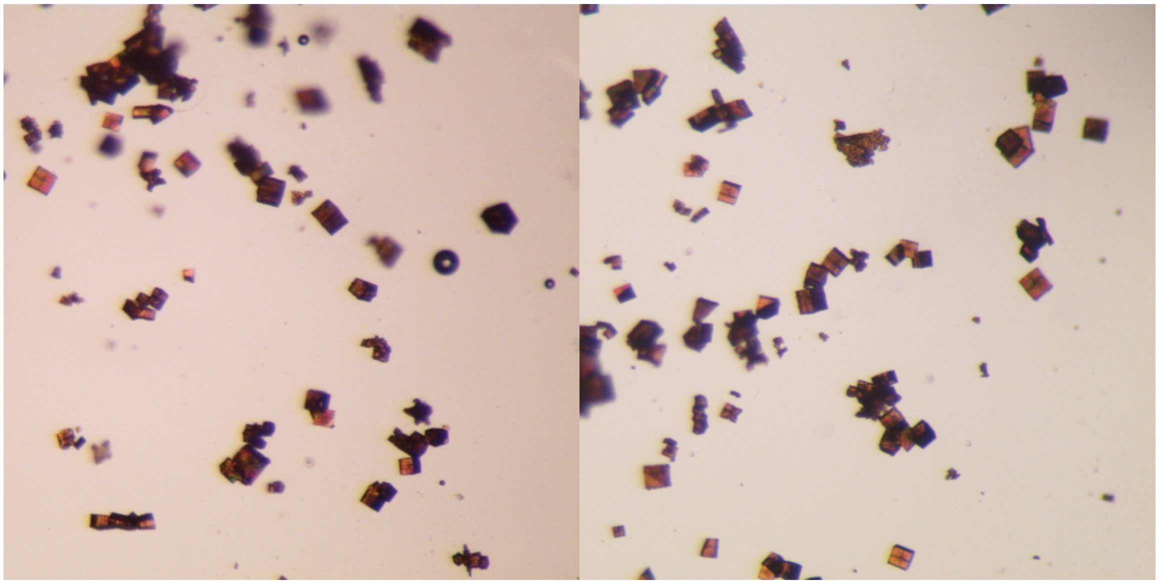

**Figure S1.** Photographs of (CYS)$PbCl_2$ single crystals. There are two crystal morphologies, plates and cubes; both give the same PXRD pattern. The plate-like crystals are visibly twinned into four domains. The SC-XRD experiments were performed using a fragment of the cuboidal crystals.

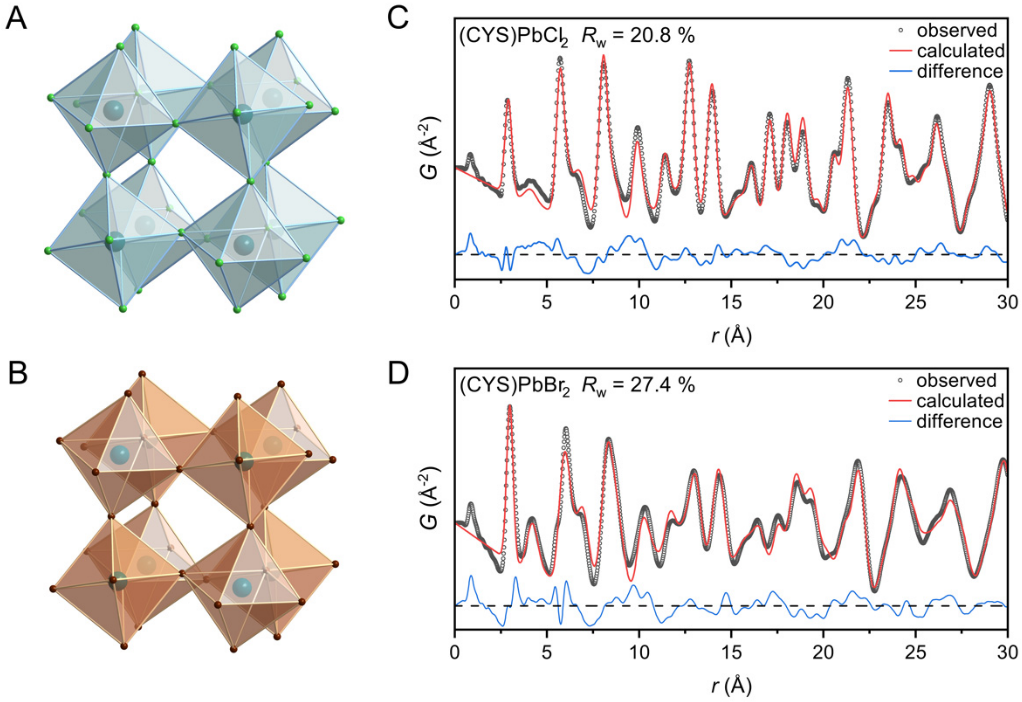

**Figure S2.** Crystal structures generated by X-ray PDF fitting of **(A)** (CYS)$PbCl_2$ and **(B)** (CYS)$PbBr_2$, only considering the inorganic lattice. X-ray PDF data and fits for **(C)** (CYS)$PbCl_2$ and **(D)** (CYS)$PbBr_2$. Turquoise, green, brown spheres represent Pb, Cl/S, and Br/S atoms, respectively. The residuals improve upon using a virtual K atom to mimic the electron density of the organoammonium tail of CYS (Figure 2).

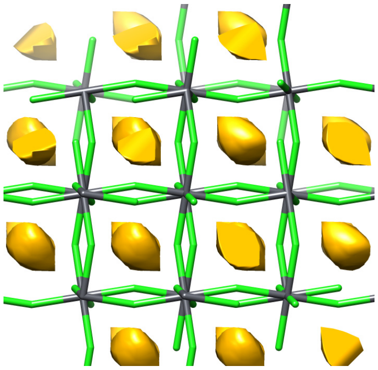

**Figure S3.** Extra electron density in the cuboctahedral cavity of the 3D perovskite (yellow) when comparing the experimental data and the inorganic lattice PDF model, calculated by differential-envelope density (DED) analysis.

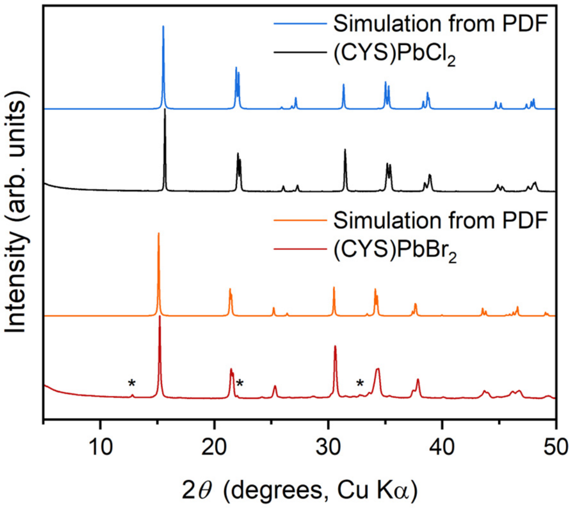

**Figure S4.** Experimental powder X-ray diffraction patterns of (CYS)PbX$_2$ (black line for X = Cl and red line for X = Br), in agreement with the simulated patterns from the PDF models. The asterisks indicate ca. 5% of the intergrowth phase in (CYS)PbBr$_2$.

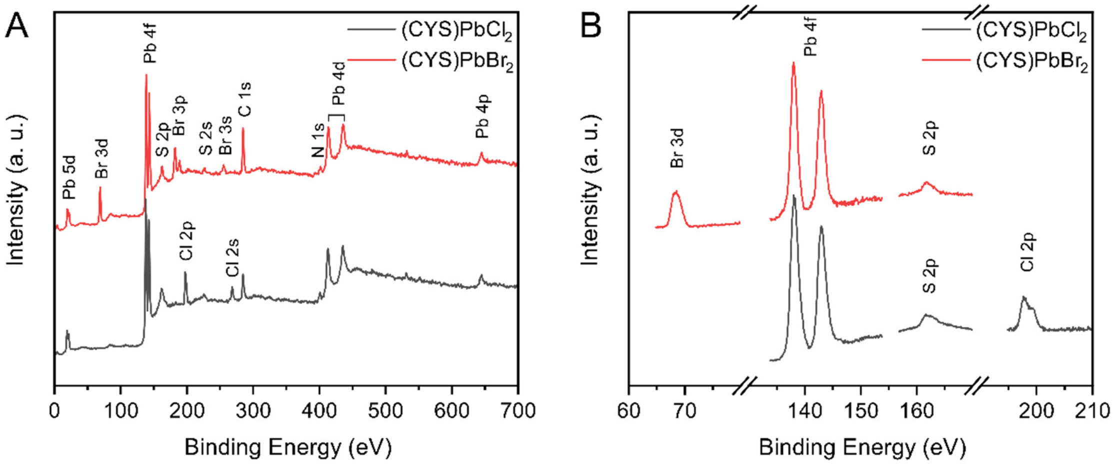

**Figure S5. (A)** XPS survey spectra of (CYS)PbX$_2$ (X = Cl, Br) powders, ranging from 0 to 700 eV. **(B)** High-resolution XPS scans for Pb 4f, S 2p, Cl 2p, and Br 3d.

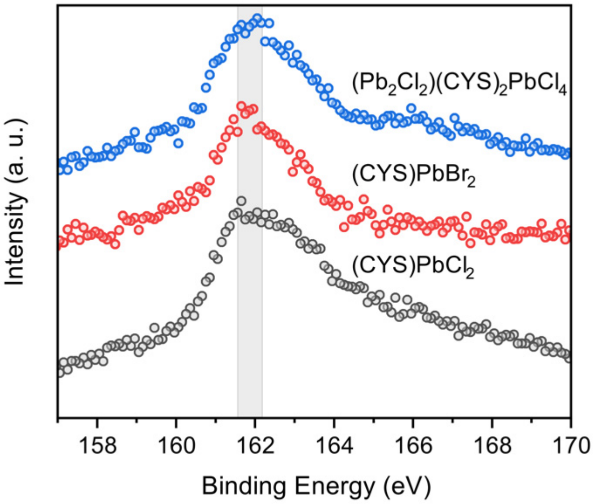

**Figure S6.** High-resolution XPS scans of S 2p: comparisons between (CYS)PbX$_2$ and the intergrowth (Pb$_2$Cl$_2$)(CYS)$_2$PbCl$_4$. The binding energy of all three materials is ca. 162 eV, corresponding to the chemical state of metal sulfide.

**Table S2.** Molar elemental ratio determined by high-resolution XPS

| Perovskites | Pb | X | S |
|---|---|---|---|
| (CYS)$PbCl_2$ | 1 | 1.7 | 0.91 |
| (CYS)$PbBr_2$ | 1 | 1.7 | 0.87 |
| ($Pb_2Cl_2$)$(CYS)_2PbCl_4$ | 1 | 2.1 | 0.76 |

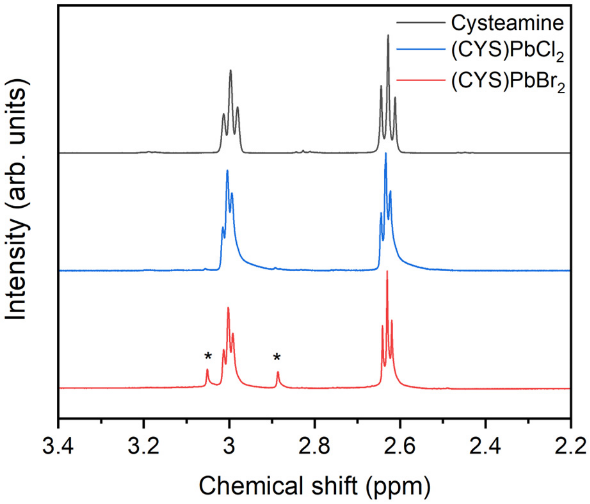

**Figure S7.** $^1$H-NMR spectra of cysteamine, (CYS)$PbCl_2$, and (CYS)$PbBr_2$ dissolved in a DCl solution in $D_2O$ (20 wt. %). The asterisks indicate impurities in the deuterium solvent due to the low solubility of (CYS)$PbBr_2$.

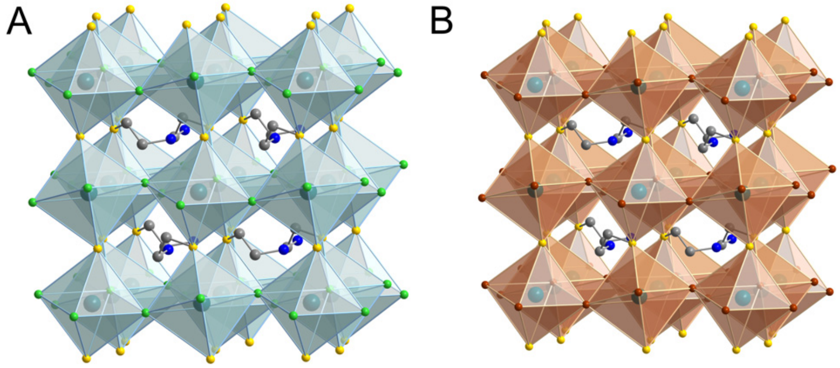

**Figure S8.** Structural models of **(A)** (CYS)$PbCl_2$ and **(B)** (CYS)$PbBr_2$ in a cubic supercell. A rhombohedral supercell with 6 formula units was used for DFT calculations. All sulfur atoms are aligned in one direction. Turquoise, green, brown, blue, gray, and yellow spheres represent Pb, Cl, Br, N, C, and S atoms. Hydrogens are omitted for clarity.

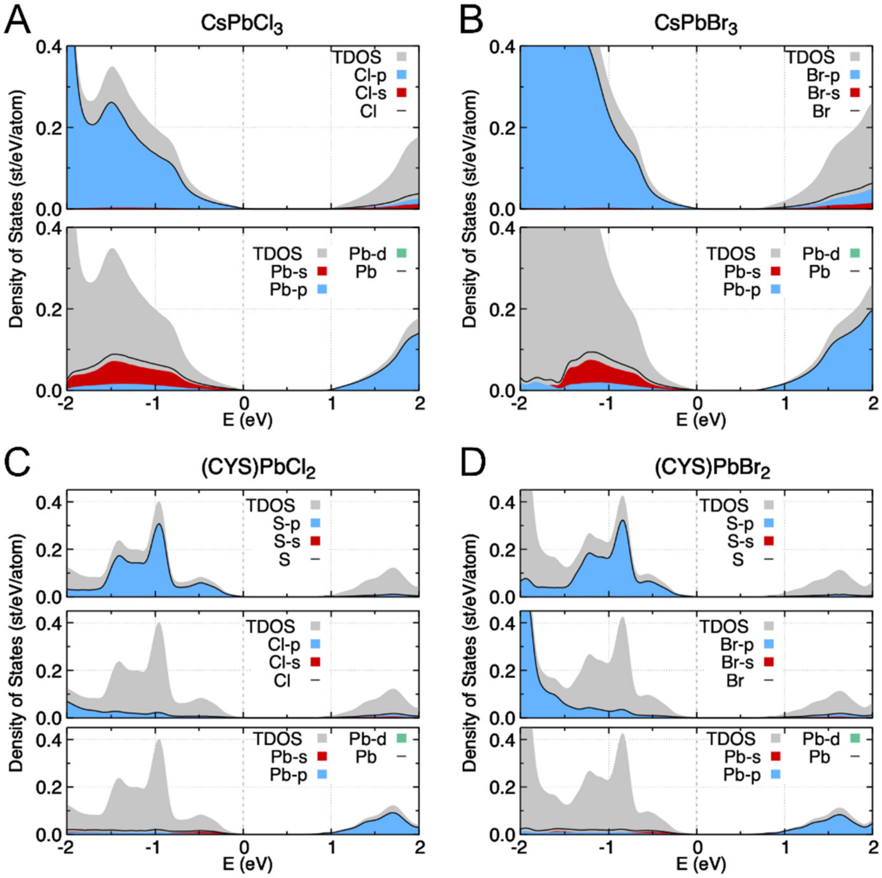

**Figure S9.** Projected total density of states (TDOS) and partial density of states calculated for (**A**) orthorhombic $CsPbCl_3$, (**B**) orthorhombic $CsPbBr_3$, (**C**) (CYS)$PbCl_2$, and (**D**) (CYS)$PbBr_2$.

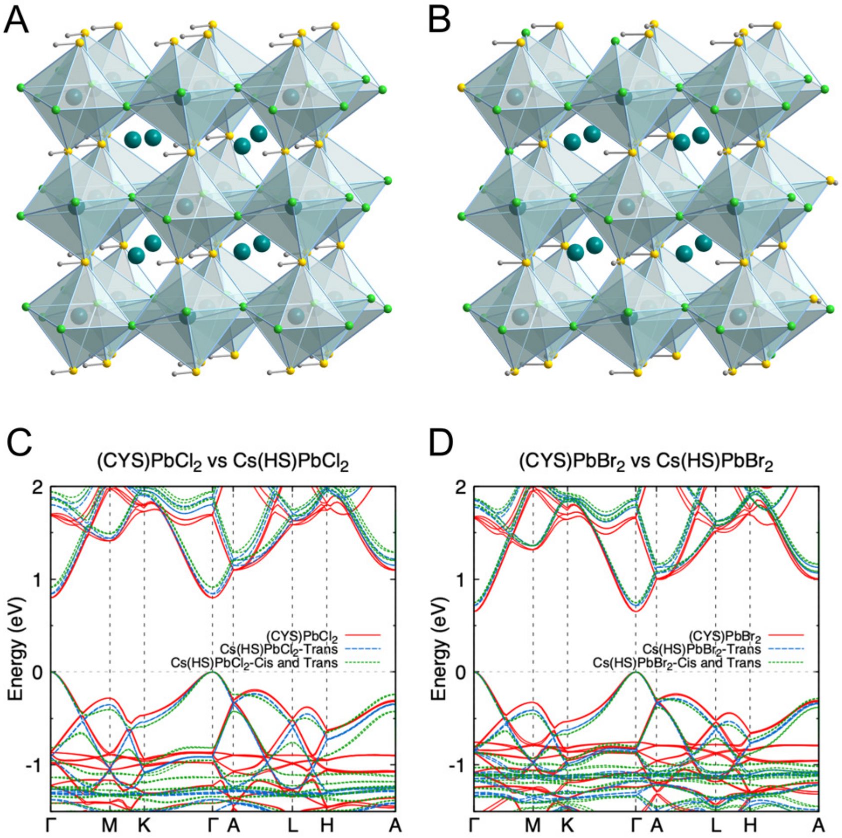

**Figure S10.** Structural models of Cs(HS)PbCl$_2$ with **(A)** *trans* and **(B)** both *cis* and *trans* ordering of the S atoms. Turquoise, teal, green, gray, and yellow spheres represent Pb, Cs, Cl, H, and S atoms, respectively. Band structures of (CYS)PbX$_2$ (red solid) and Cs(HS)PbX$_2$ model structures with *trans* (blue dashed) and both *cis* and *trans* (green dashed) ordering of S atoms for **(C)** X = Cl and **(D)** X = Br in a rhombohedral supercell. Band structures are aligned to the valence band maxima for clarity.

**Table S3.** Summary of calculated band structures

| Structures | Band gap[a] (eV) | VBM contributions[b] | | | CBM contributions[b] | | |
|---|---|---|---|---|---|---|---|
| | | S | X | Pb | S | X | Pb |
| Orthorhombic $CsPbCl_3$ | 1.00 | 0.00 | 0.34 | 0.66 | 0.00 | 0.00 | 1.00 |
| Orthorhombic $CsPbBr_3$ | 0.72 | 0.00 | 0.43 | 0.57 | 0.00 | 0.00 | 1.00 |
| $(CYS)PbCl_2$ | 0.80 | 0.68 | 0.03 | 0.29 | 0.00 | 0.00 | 1.00 |
| $(CYS)PbBr_2$ | 0.65 | 0.60 | 0.07 | 0.33 | 0.00 | 0.00 | 1.00 |
| $Cs(HS)PbCl_2$[c] | 0.84 (0.91) | 0.58 | 0.05 | 0.37 | 0.00 | 0.00 | 1.00 |
| $Cs(HS)PbBr_2$[c] | 0.72 (0.75) | 0.46 | 0.11 | 0.43 | 0.00 | 0.00 | 1.00 |

[a] The bandgap values were calculated by PBE-SOC.

[b] The calculated contribution of individual atoms to the VBM and CBM at the Gamma point (in fraction).

[c] The values in parenthesis were calculated using $Cs(HS)PbX_2$ models with *cis* and *trans* ordering of S atoms. The rest were calculated from $Cs(HS)PbX_2$ models with *trans* ordering of S atoms.

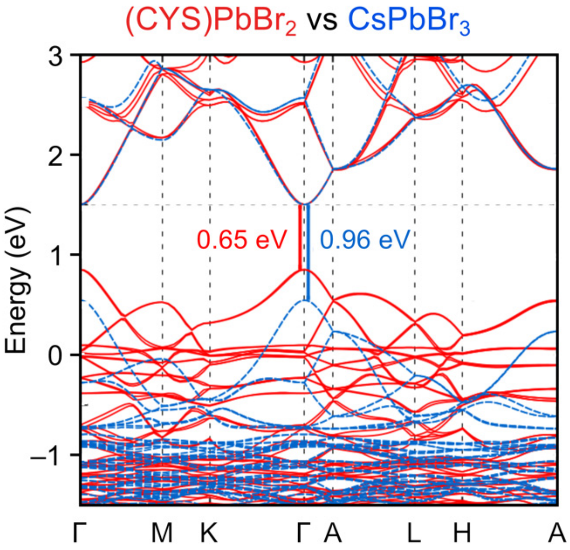

**Figure S11.** Comparison of the band structures of $(CYS)PbBr_2$ and hypothetical $CsPbBr_3$, both in the *R*-3*c* space group. The conduction band minima have been arbitrarily aligned for easier comparison of band dispersion.

**Table S4.** Summary of calculated effective masses

| Structures | Hole effective mass (VBM) | | | | | Electron effective mass (CBM) | | | | |
|---|---|---|---|---|---|---|---|---|---|---|
| | $m^*_{h11}$ | $m^*_{h22}$ | $m^*_{h33}$ | $<m^*_h>^a$ | Std. Dev. | $m^*_{e11}$ | $m^*_{e22}$ | $m^*_{e33}$ | $<m^*_e>^a$ | Std. Dev. |
| Orthorhombic $CsPbCl_3$ | 0.172 | 0.192 | 0.200 | 0.187 | 0.012 | 0.215 | 0.212 | 0.188 | 0.204 | 0.012 |
| Orthorhombic $CsPbBr_3$ | 0.139 | 0.154 | 0.165 | 0.152 | 0.011 | 0.163 | 0.160 | 0.139 | 0.153 | 0.011 |
| Rhombohedral $CsPbCl_3$ | 0.303 | 0.303 | 0.325 | 0.310 | 0.010 | 0.314 | 0.313 | 0.309 | 0.312 | 0.002 |
| Rhombohedral $CsPbBr_3$ | 0.205 | 0.206 | 0.222 | 0.211 | 0.008 | 0.214 | 0.213 | 0.203 | 0.210 | 0.005 |
| $(CYS)PbCl_2$ | 0.116 | 0.568 | 0.683 | 0.253 | 0.318 | 0.363 | 0.292 | 0.216 | 0.277 | 0.061 |
| $(CYS)PbBr_2$ | 0.132 | 0.340 | 0.374 | 0.227 | 0.120 | 0.228 | 0.226 | 0.205 | 0.219 | 0.010 |
| *trans* $Cs(HS)PbCl_2$ | 0.108 | 0.496 | 0.539 | 0.228 | 0.247 | 0.606 | 0.448 | 0.329 | 0.433 | 0.117 |
| *trans* $Cs(HS)PbBr_2$ | 0.128 | 0.278 | 0.313 | 0.205 | 0.089 | 0.359 | 0.254 | 0.239 | 0.275 | 0.054 |
| *cis* and *trans* $Cs(HS)PbCl_2$ | 0.137 | 0.422 | 0.537 | 0.260 | 0.198 | 0.469 | 0.403 | 0.311 | 0.383 | 0.066 |
| *cis* and *trans* $Cs(HS)PbBr_2$ | 0.141 | 0.258 | 0.309 | 0.211 | 0.075 | 0.317 | 0.236 | 0.233 | 0.257 | 0.039 |

[a] Reported effective mass values are the harmonic mean over the three eigenvalues of the effective mass tensor.

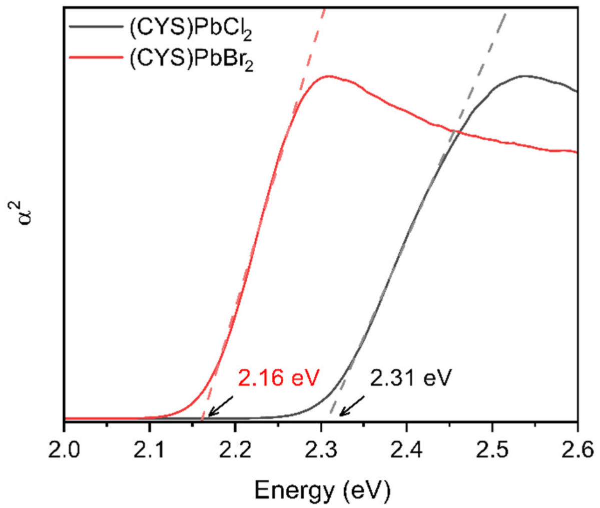

**Figure S12.** Tauc plot of $\alpha^2$ vs. energy to determine the optical bandgaps of (CYS)PbX$_2$ for a direct-gap semiconductor ($\alpha$ = pseudo-absorbance). Fits to the linear portion of the plot give the direct bandgap values of 2.31 eV and 2.16 eV for X = Cl and Br, respectively.

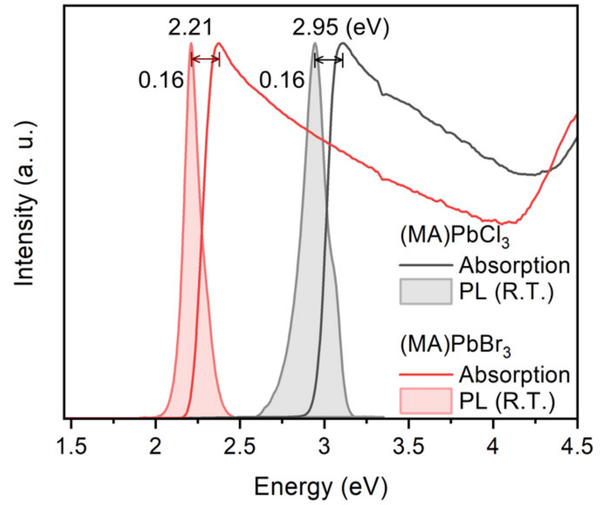

**Figure S13.** Room-temperature photoluminescence (PL; shaded) and diffuse reflectance spectra of (MA)PbX$_3$ powders. The PL peaks locate at 2.95 and 2.21 eV for X = Cl and Br, respectively (excitation wavelength: 340 nm).

**Table S5.** Summary of optical properties

| Perovskites | *T* (K) | PL peak center (eV) | Stokes shift (eV) | FWHM (eV) |
|---|---|---|---|---|
| (MA)$PbCl_3$ | 298 | 2.95 | 0.16 | 0.16 |
| (MA)$PbBr_3$ | 298 | 2.21 | 0.16 | 0.11 |
| (CYS)$PbCl_2$ | 80 | 1.98 | 0.56 | 0.54 |
| (CYS)$PbBr_2$ | 80 | 1.66 | 0.64 | 0.46 |

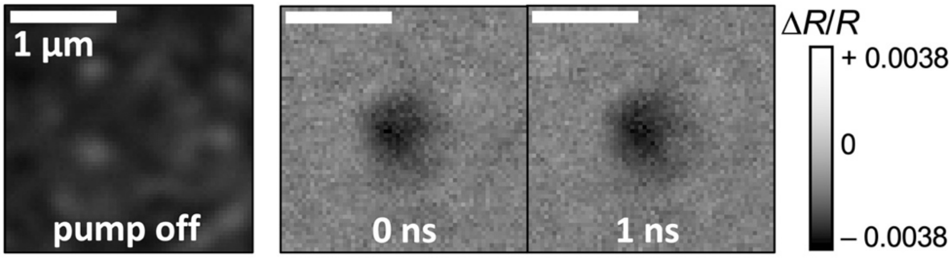

**Figure S14.** Representative ground-state scattering image (pump off) and stroboSCAT time series. The region of dark contrast in the $\Delta R/R$ images corresponds to the excited carrier profile.

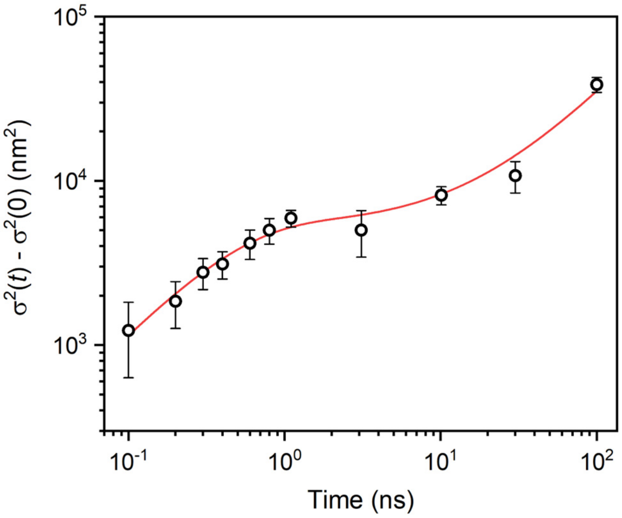

**Figure S15.** Mean-squared expansion curve over the full stroboSCAT time window, fit to a model that contains two diffusion coefficients as explained in the supplementary discussion.

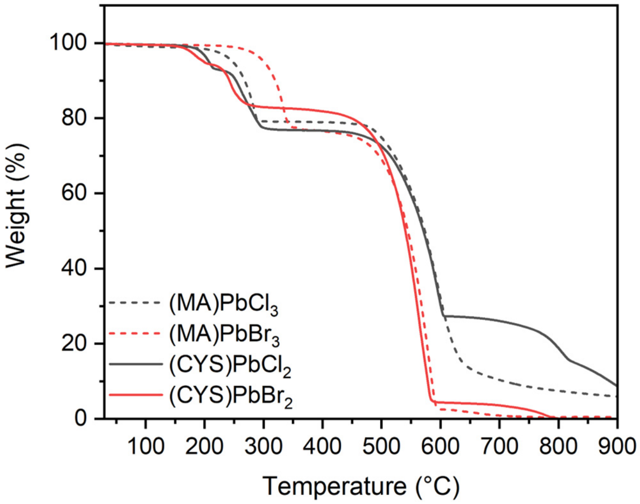

**Figure S16.** Thermogravimetric analyses of (CYS)PbX$_2$ and (MA)PbX$_3$ at a scan rate of 1 °C/minute, measuring from room temperature to 900 °C.

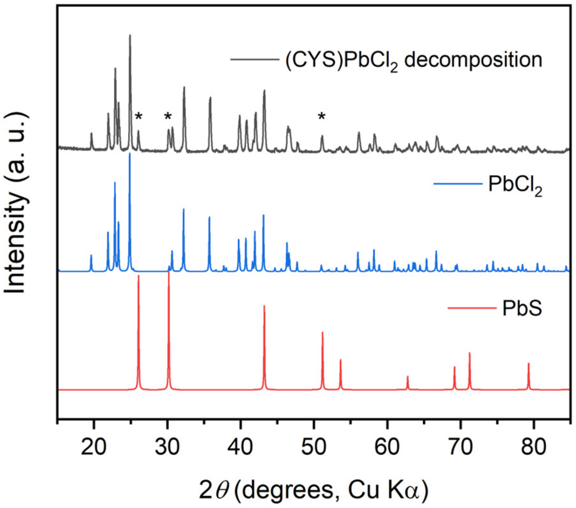

**Figure S17.** Comparison of PXRD patterns of the (CYS)PbCl$_2$ thermal decomposition product at 350 °C, PbCl$_2$, and PbS. The asterisks indicate peaks from PbS.

**Table S6.** Summary of thermal properties from TGA

| Perovskites | $T_d$ (°C) | theoretical value [a] | experimental value [b] |
|---|---|---|---|
| $(MA)PbCl_3$ | 248.1 | 80.5% | 79.1% |
| $(MA)PbBr_3$ | 300.9 | 76.6% | 76.9% |
| $(CYS)PbCl_2$ | 207.1 | 78.3% | 77.0% |
| $(CYS)PbBr_2$ | 199.0 | 82.6% | 82.7% |

[a] The theoretical weight percentage of $PbX_2$ in the formula

[b] The weight percentage of residues after the first decomposition step

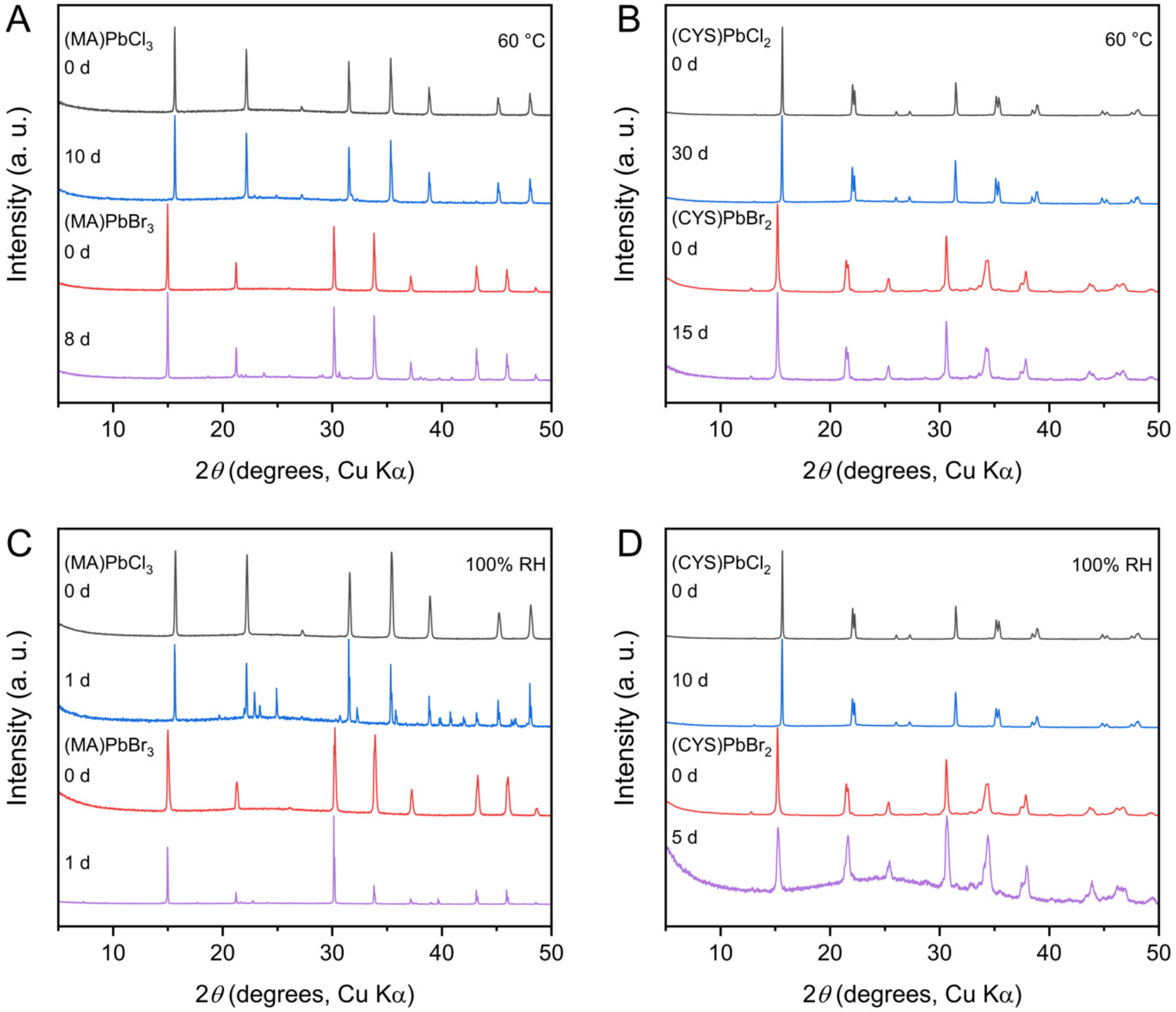

**Figure S18.** PXRD patterns of **(A)** $(MA)PbX_3$ and **(B)** $(CYS)PbX_2$ powders after heating at 60 °C in air. PXRD patterns of **(C)** $(MA)PbX_3$ and **(D)** $(CYS)PbX_2$ after exposure to 100% relative humidity in the dark.

## 5. Reference

(1) Chen, K.; Deng, X.; Goddard, R.; Tüysüz, H. Pseudomorphic Transformation of Organometal Halide Perovskite Using the Gaseous Hydrogen Halide Reaction. *Chem. Mater.* **2016**, *28* (15), 5530–5537.

(2) Aubrey, M. L.; Saldivar Valdes, A.; Filip, M. R.; Connor, B. A.; Lindquist, K. P.; Neaton, J. B.; Karunadasa, H. I. Directed Assembly of Layered Perovskite Heterostructures as Single Crystals. *Nature* **2021**, *597* (7876), 355–359.

(3) Bruker, APEX. SAINT and SADABS Bruker AXS Inc. *Madison, Wisconsin, USA* **2007**.

(4) Sheldrick, G. M. SHELXT – Integrated Space-Group and Crystal-Structure Determination. *Acta Cryst. A* **2015**, *71* (1), 3–8.

(5) Sheldrick, G. M. Crystal Structure Refinement with SHELXL. *Acta Cryst. C* **2015**, *71* (1), 3–8.

(6) Dolomanov, O. V.; Bourhis, L. J.; Gildea, R. J.; Howard, J. a. K.; Puschmann, H. OLEX2: A Complete Structure Solution, Refinement and Analysis Program. *J. Appl. Cryst.* **2009**, *42* (2), 339–341.

(7) van der Sluis, P.; Spek, A. L. BYPASS: An Effective Method for the Refinement of Crystal Structures Containing Disordered Solvent Regions. *Acta Cryst. A* **1990**, *46* (3), 194–201.

(8) Toby, B. H.; Von Dreele, R. B. GSAS-II: The Genesis of a Modern Open-Source All Purpose Crystallography Software Package. *J Appl Cryst* **2013**, *46* (2), 544–549.

(9) Yang, X.; Juhas, P.; Farrow, C. L.; Billinge, S. J. L. XPDFsuite: An End-to-End Software Solution for High Throughput Pair Distribution Function Transformation, Visualization and Analysis. *arXiv:1402.3163v3*, **2014**, 1–4.

(10) Farrow, C. L.; Juhas, P.; Liu, J. W.; Bryndin, D.; Boin, E. S.; Bloch, J.; Proffen, T.; Billinge, S. J. L. PDFfit2 and PDFgui: Computer Programs for Studying Nanostructure in Crystals. *J. Phys. Condens. Matter.* **2007**, *19* (33).

(11) Yakovenko, A. A.; Wei, Z.; Wriedt, M.; Li, J. R.; Halder, G. J.; Zhou, H. C. Study of Guest Molecules in Metal-Organic Frameworks by Powder X-Ray Diffraction: Analysis of Difference Envelope Density. *Cryst. Growth Des.* **2014**, *14* (11), 5397–5407.

(12) Chapman, K. W.; Chupas, P. J.; Kepert, C. J. Selective Recovery of Dynamic Guest Structure in a Nanoporous Prussian Blue through in Situ X-Ray Diffraction: A Differential Pair Distribution Function Analysis. *J. Am. Chem. Soc.* **2005**, *127* (32), 11232–11233.

(13) Kubelka, P.; Munk, F. Z. Ein Beitrag Zur Optik Der Farbanstriche. *Zeitschrift fur Technische Physik* **1931**, *12*, 593–601.

(14) Delor, M.; Weaver, H. L.; Yu, Q.; Ginsberg, N. S. Imaging Material Functionality through Three-Dimensional Nanoscale Tracking of Energy Flow. *Nat. Mater.* **2020**, *19* (1), 56–62.

(15) Schneider, C. A.; Rasband, W. S.; Eliceiri, K. W. NIH Image to ImageJ: 25 Years of Image Analysis. *Nat. Methods* **2012**, *9* (7), 671–675.

(16) Giannozzi, P.; Andreussi, O.; Brumme, T.; Bunau, O.; Nardelli, M. B.; Calandra, M.; Car, R.; Cavazzoni, C.; Ceresoli, D.; Cococcioni, M.; Colonna, N.; Carnimeo, I.; Corso, A. D.; Gironcoli, S. de; Delugas, P.; DiStasio, R. A.; Ferretti, A.; Floris, A.; Fratesi, G.; Fugallo, G.; Gebauer, R.; Gerstmann, U.; Giustino, F.; Gorni, T.; Jia, J.; Kawamura, M.; Ko, H.-Y.; Kokalj, A.; Küçükbenli, E.; Lazzeri, M.; Marsili, M.; Marzari, N.; Mauri, F.; Nguyen, N. L.; Nguyen, H.-V.; Otero-de-la-Roza, A.; Paulatto, L.; Poncé, S.; Rocca, D.; Sabatini, R.; Santra, B.; Schlipf, M.; Seitsonen, A. P.; Smogunov, A.; Timrov, I.; Thonhauser, T.; Umari, P.; Vast, N.; Wu, X.; Baroni, S. Advanced Capabilities for Materials Modelling with Quantum ESPRESSO. *J. Phys.: Condens. Matter.* **2017**, *29* (46), 465901.

(17) Perdew, J. P.; Burke, K.; Ernzerhof, M. Generalized Gradient Approximation Made Simple. *Phys. Rev. Lett.* **1996**, *77* (18), 3865–3868.

(18) Hamann, D. R. Optimized Norm-Conserving Vanderbilt Pseudopotentials. *Phys. Rev. B* **2013**, *88* (8), 085117.

(19) van Setten, M. J.; Giantomassi, M.; Bousquet, E.; Verstraete, M. J.; Hamann, D. R.; Gonze, X.; Rignanese, G.-M. The PseudoDojo: Training and Grading a 85 Element Optimized Norm-Conserving Pseudopotential Table. *Comput. Phys. Commun.* **2018**, *226*, 39–54.

(20) Monkhorst, H. J.; Pack, J. D. Special Points for Brillouin-Zone Integrations. *Phys. Rev. B* **1976**, *13* (12), 5188–5192.

(21) A. Fonari, C. Sutton, Effective Mass Calculator, **2012**.

(22) Linaburg, M. R.; McClure, E. T.; Majher, J. D.; Woodward, P. M. $Cs_{1-x}Rb_xPbCl_3$ and $Cs_{1-x}Rb_xPbBr_3$ Solid Solutions: Understanding Octahedral Tilting in Lead Halide Perovskites. *Chem. Mater.* **2017**, *29* (8), 3507–3514.

(23) Cooper, J. K.; Reyes-Lillo, S. E.; Hess, L. H.; Jiang, C.-M.; Neaton, J. B.; Sharp, I. D. Physical Origins of the Transient Absorption Spectra and Dynamics in Thin-Film Semiconductors: The Case of $BiVO_4$. *J. Phys. Chem. C* **2018**, *122* (36), 20642–20652.

(24) Utterback, J. K.; Sood, A.; Coropceanu, I.; Guzelturk, B.; Talapin, D. V.; Lindenberg, A. M.; Ginsberg, N. S. Nanoscale Disorder Generates Subdiffusive Heat Transport in Self-Assembled Nanocrystal Films. *Nano Lett.* **2021**, *21* (8), 3540–3547.

(25) Delor, M.; Slavney, A. H.; Wolf, N. R.; Filip, M. R.; Neaton, J. B.; Karunadasa, H. I.; Ginsberg, N. S. Carrier Diffusion Lengths Exceeding 1 μm Despite Trap-Limited Transport in Halide Double Perovskites. *ACS Energy Lett.* **2020**, *5* (5), 1337–1345.

(26) Folie, B. D.; Tan, J. A.; Huang, J.; Sercel, P. C.; Delor, M.; Lai, M.; Lyons, J. L.; Bernstein, N.; Efros, A. L.; Yang, P.; Ginsberg, N. S. Effect of Anisotropic Confinement on Electronic Structure and Dynamics of Band Edge Excitons in Inorganic Perovskite Nanowires. *J. Phys. Chem. A* **2020**, *124* (9), 1867–1876.

(27) Haeger, T.; Heiderhoff, R.; Riedl, T. Thermal Properties of Metal-Halide Perovskites. *J. Mater. Chem. C* **2020**, *8* (41), 14289–14311.

(28) Akbulatov, A. F.; Martynenko, V. M.; Frolova, L. A.; Dremova, N. N.; Zhidkov, I.; Tsarev, S. A.; Luchkin, S. Y.; Kurmaev, E. Z.; Aldoshin, S. M.; Stevenson, K. J.; Troshin, P. A. Intrinsic Thermal Decomposition Pathways of Lead Halide Perovskites $APbX_3$. *Sol. Energy Mater. Sol. Cells* **2020**, *213*, 110559.